scientific reports

Check for updates

OPEN

Consistency of spectral results in cardiac dual-source photon-counting CT

Leening P. Liu[1,2]✉, Nadav Shapira[1], Pooyan Sahbaee[3], Grace J. Gang[1], Friedrich D. Knollman[1], Marcus Y. Chen[4], Harold I. Litt[1] & Peter B. Noël[1,5]✉

We evaluate stability of spectral results at different heart rates, acquisition modes, and cardiac phases in first-generation clinical dual-source photon-counting CT (PCCT). A cardiac motion simulator with a coronary stenosis mimicking a 50% eccentric calcium plaque was scanned at five different heart rates (0, 60–100 bpm) with the three available cardiac scan modes (high pitch prospectively ECG-triggered spiral, prospectively ECG-triggered axial, retrospectively ECG-gated spiral). Subsequently, full width half max (FWHM) of the stenosis, Dice score (DSC) for the stenosed region, and eccentricity of the non-stenosed region were calculated for virtual monoenergetic images (VMI) at 50, 70, and 150 keV and iodine density maps at both diastole and systole. FWHM averaged differences of − 0.20, − 0.28, and − 0.15 mm relative to static FWHM at VMI 150 keV across acquisition parameters for high pitch prospectively ECG-triggered spiral, prospectively ECG-triggered axial, and retrospectively ECG-gated spiral scans, respectively. Additionally, there was no effect of heart rate and acquisition mode on FWHM at diastole (p-values < 0.001). DSC demonstrated similarity among parameters with standard deviations of 0.08, 0.09, 0.11, and 0.08 for VMI 50, 70, and 150 keV, and iodine density maps, respectively, with insignificant differences at diastole (p-values < 0.01). Similarly, eccentricity illustrated small differences across heart rate and acquisition mode for each spectral result. Consistency of spectral results at different heart rates and acquisition modes for different cardiac phase demonstrates the added benefit of spectral results from PCCT to dual-source CT to further increase confidence in quantification and advance cardiovascular diagnostics.

Abbreviations

CT	Computed tomography
Spiral	Retrospective low-pitch helical
Sequence	Prospective step-and-shoot
Flash	Prospective high pitch helical
PCCT	Photon counting CT
VMI	Virtual monoenergetic images
35%	Systole
70%	Diastole
QIR	Quantum iterative reconstruction
$CTDI_{vol}$	Volumetric CT dose index
FWHM	Full width half max
DSC	Dice similarity coefficient
ANOVA	Analysis of variance

ECG-synchronized computed tomography angiography (CTA) has become an increasingly vital diagnostic tool for cardiovascular disease[1]. CTA is utilized to determine the risk of heart disease and to identify coronary stenoses[2,3]. It can also be used to detect abnormal structures such as valve vegetations/calcifications, aortic dissection, and aneurysms. Technological advances have increased its utility and resulted in a shift in clinical

[1]Department of Radiology, University of Pennsylvania, Philadelphia, PA, USA. [2]Department of Bioengineering, University of Pennsylvania, Philadelphia, PA, USA. [3]Siemens Healthineers, Malvern, PA, USA. [4]National Heart, Lung, and Blood Institute, Bethesda, MD, USA. [5]Department of Diagnostic and Interventional Radiology, School of Medicine & Klinikum rechts der Isar, Technical University of Munich, 81675 Munich, Germany. ✉email: leening.liu@pennmedicine.upenn.edu; pbnoel@upenn.edu

day-to-day routine[4]. For example, for patients with stable chest pain, coronary CT angiography has shown excellent accuracy compared to catheter-based coronary angiography without the invasive nature[5]. In addition, development of different acquisition modes[6] and technological advancements, such as dual source CT[7], have addressed radiation dose exposure and temporal resolution concerns associated with retrospective low-pitch helical (spiral) acquisitions.

In dual source CT, an additional X-ray source and detector set is located approximately 90° from the first X-ray source and detector. As a result of this addition, the temporal resolution is effectively doubled since the rotation required to acquire the needed data is reduced by half. This improved temporal resolution has resulted in better image quality for existing acquisition modes, especially at higher heart rates where increased motion increases the likelihood of motion-related artifacts[8], but also enables a new acquisition mode, prospective high pitch helical (flash), which takes advantage of the two sources[9]. This mode can significantly reduce radiation dose in comparison to spiral and prospective step-and-shoot (sequence) but limits retrospective reconstruction capabilities and is most effective at low heart rates[9].

Spectral CT provides additional quantitative data in cardiac CT, including material maps, that are valuable for diagnostic assessments. Photon counting CT (PCCT), the most recent realization of spectral CT, makes quantitative maps available for cardiac imaging with reduced noise, stability at low doses, increased contrast to noise ratio, and high spatial resolution in prototype and clinical PCCT scanners compared to dual energy CT[10–13]. Iodine density maps separate the iodine signal for the visualization of perfusion and vascular structures[14,15] and can also be analyzed quantitatively to characterize lesions, i.e. cysts vs. hepatocellular carcinoma[16]. Additionally, virtual non-contrast images can obviate the need for an additional true non-contrast scan[17]. Virtual monoenergetic images (VMI) can improve contrast at lower energies and separate materials of different densities at higher energies while also reducing the deleterious effects of high density materials, i.e. calcium blooming and metal artifacts[18].

The first clinical PCCT combines dual source CT and photon-counting detectors. This study assessed the stability of spectral results of a clinical dual-source PCCT for different acquisition modes and cardiac phases using a cardiac motion phantom with elements simulating a coronary lumen with and without a calcified stenosis.

Materials and methods

Phantom. To evaluate the effect of acquisition mode, cardiac phase, and heart rate on spectral results, a cardiac motion simulator (Sim4D-VL, Quality Assurance in Radiology and Medicine, Möhrendorf, Germany) that replicated coronary artery movement was utilized (Fig. 1)[19]. A set of 3 mm diameter rods mimicking coronary stenoses of different materials and severity was submerged in water and surrounded with a cardiac phantom (Cardio QRM, Quality Assurance in Radiology and Medicine, Möhrendorf, Germany) and extension ring (Fig. 1B). Specifically, analysis was performed for the stenosis with an eccentric calcium plaque measuring a diameter of 1.5 mm and a length of 1.0 cm, covering 50% of rod area and comprising 373 mg/cm^3 hydroxyapatite (Fig. 1C). The iodinated lumen measured approximately 350 HU, while the calcium plaque measured approximately 415 HU.

Image acquisition. The phantom was scanned with a first-generation dual-source PCCT (NAEOTOM Alpha, Siemens Healthineers, Erlangen, Germany) in the three available ECG-synchronized modes: dual-source low-pitch retrospective helical (spiral), dual-source prospective step-and-shoot (sequence), and dual-source high pitch prospective helical (flash) at different heart rates (0, 60, 70, 80, and 100 beats per minute). Specifically at 0 bpm, the cardiac motion simulator was turned off, and the scanner's virtual ECG at 60 bpm was utilized to trigger the scan for the different scan modes. Scans were performed at a tube voltage of 120 kVp at a fixed effective exposure of 30 mAs to match noise between scan modes (~22 HU on VMI 70 keV). This exposure corresponded to average volumetric CT dose index ($CTDI_{vol}$) of 20, 13, and 2 mGy for spiral, sequence, and flash, respectively. While both spiral and sequence scans allowed for reconstruction at systole (35%) and diastole (70%) with a single scan because scans encompassed systole to diastole (35–70%), separate flash scans were required for cardiac phases of 35% and 70%. To ensure the stenosis was imaged at 35% and 70% with flash

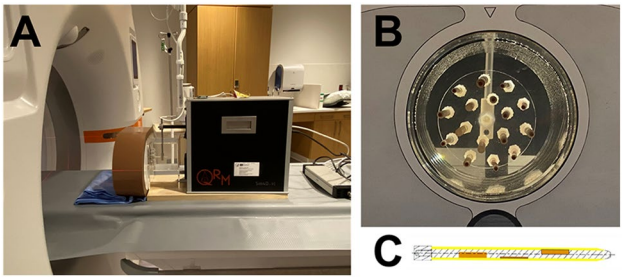

Figure 1. Experimental set up. A cardiac motion phantom was scanned with a dual-source photon-counting CT (**A**). The phantom included rods mimicking coronary stenoses of different materials (**B**) and extents (**C**) represented in a cross section through the center of the rod. Orange regions correspond to the stenosis while the yellow region corresponds to outer vessel walls.

scans, the location of the center of the stenosis was determined relative to the scan range, and the cardiac phase range at each heart rate was adjusted to ensure the center of the stenosis was scanned at the appropriate cardiac phase (35% or 70%). Subsequently, at each acquisition mode, cardiac phase, and heart rate combination, spectral results will be reconstructed with a slice thickness of 0.4 mm at 0.4 mm intervals, field of view of 200 mm, reconstruction kernel of Bv36, matrix size of 512 × 512, and quantum iterative reconstruction (QIR) level of 2. Specifically, VMI 50, 70, and 150 keV as well as iodine density maps were reconstructed to cover the range of VMI energies while also including iodine quantification. These parameters matched clinical protocols used at our institution. Other relevant scan and reconstruction parameters are included in Table 1.

Image analysis. To characterize the reliability of imaging of the stenosed and non-stenosed regions across acquisition mode, cardiac phase, and heart rate, quantitative metrics were investigated to describe size and similarity of the stenosed region as well as shape of the non-stenosed region. First, the center of the stenosis range was automatically determined to ensure that the approximate same area of the stenosis was analyzed between scans. Because the lumen and calcified stenosis were similar on all spectral results except VMI 150 keV, adaptive thresholding was applied to the imaging volume of VMI 150 keV with adaptiveThreshold from the OpenCV package. The range of axial slices with the cross-section of the stenosis was determined and the center calculated. Then, to establish the similarity in the rod width at different acquisition modes, cardiac phases, and heart rates, line profiles with a length of 30 pixels (11.72 mm) were extracted from axial slices and centered on the stenosis to include the peak from the stenosis as well as the adjacent background. The isolation of the stenosis from the noisy background was achieved by implementing a threshold determined using the mean plus standard deviation of the first five and last five values of the line profile. Consequently, this process eliminated the noisy background and isolated the segment of the line profile associated with the stenosis. Utilizing this peak, the width at half the peak's height, known as the full width at half maximum (FWHM), was calculated for each parameter set and spectral result, providing a measure of the stenosis width. FWHM was reported as mean and standard deviation over 5 consecutive axial slices that included the stenosis. The same slices were maintained across different spectral results for the same acquisition parameters. Values were plotted for each spectral result individually, and average differences relative to the static FWHM were calculated.

For determining the similarity to static scans, five central axial slices of the stenosis were subjected to adaptive thresholding at each acquisition mode, heart rate, and phase for each spectral result to generate a mask. The mask for the static case (0 bpm) was then utilized to calculate the Dice similarity coefficient (DSC) for scans at the corresponding acquisition mode but different heart rate and cardiac phase, including another static scan (Fig. 2). In addition, DSC was also calculated for an additional static case (0 bpm) to assess variability between static scans. For each set of parameters, DSC was reported as mean and standard deviation across the five slices for each spectral result and visualized in a scatter plot. Standard deviation across all parameters for each spectral result as well as standard deviation across heart rate for combinations of spectral result, cardiac phase, and acquisition mode were also calculated.

Similarly, the non-stenosed regions were assessed for consistency between static and dynamic scans, by comparing eccentricity of the rod from the static circle. Eccentricity also served as an indicator of motion blurring. Eccentricity was only evaluated on VMI 50 and 70 keV and iodine density maps but not for VMI 150 keV. As iodine contrast reduces at higher VMI energies, the non-stenosed region on VMI 150 keV was not distinguishable from the background (water). Therefore, adaptive thresholding was applied to five axial slices at VMI 50 and 70 keV and iodine density maps. The contour of the generated mask was then fitted to an ellipse to determine the major and minor axes (Fig. 3). Eccentricity was then calculated as:

$$c = \sqrt{1 - \left(\frac{b}{a}\right)^2},$$

	Spiral	Sequence	Flash
Tube voltage (kVp)	120		
Pitch	0.23	N/A	3.2
Exposure (mAs)	30		
CTDIvol (mGy)	20	13	2
Collimation (mm)	0.4/57.6 (single/total)		
Slice thickness (mm)	0.14		
Convolution kernel	Bv36		
Iterative reconstruction level	QIR 2		
Field of view (mm)	200		
Matrix size	512 × 512		
Pixel spacing (mm)	0.39		

Table 1. Acquisition and reconstruction parameters for different acquisition modes.

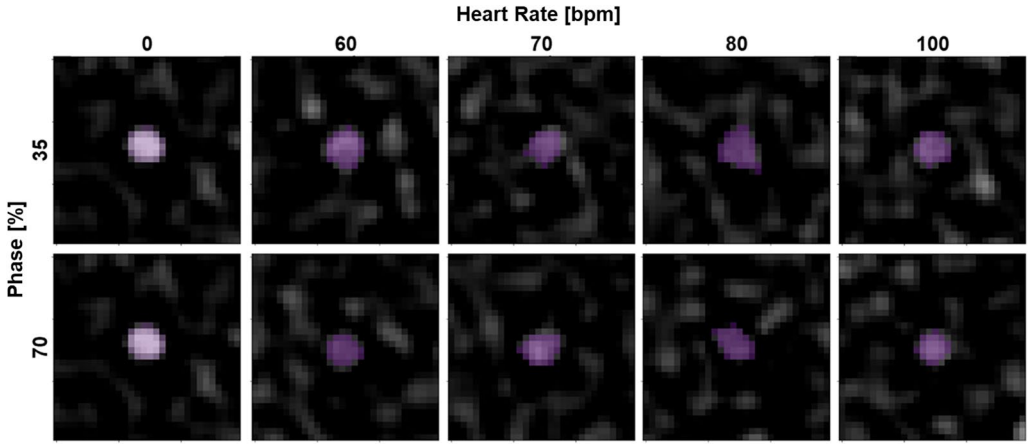

Figure 2. Adaptive thresholding of stenosis on VMI 150 keV images at varying cardiac phases and heart rates with spiral mode. Stenoses at different phases and heart rates were isolated with adaptive thresholding (purple) and demonstrated similar shape and size in comparison to the static scan (0 bpm).

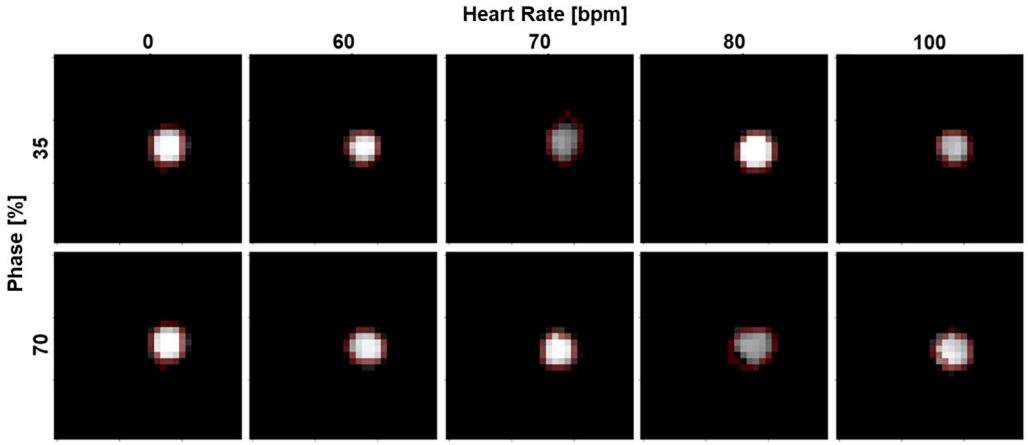

Figure 3. Shape evaluation of shape for non-stenosed region of the rod with spiral mode. Ellipse (red) were fitted to rods isolated from adaptive thresholding. At different phases and heart rates, the shape of the rod remained the same with some distortion at higher heart rates.

where c is eccentricity, b is radius of the minor axis, and a is the radius of the major axis. An eccentricity of 1 denoted a line, while an eccentricity of 0 denoted a circle. It was represented in a scatter plot with mean and standard deviation across 5 slices for each spectral result, acquisition mode, cardiac phase, and heart rate combination. The range of dynamic values and average difference from eccentricity measured in the static scan were evaluated. All image processing and analysis were performed in Python (Python Software Foundation).

Statistical analysis. For all three metrics, Shapiro–Wilk tests were used to test for normality. Then, a three-way analysis of variance (ANOVA) was performed to assess the effect of acquisition mode, cardiac phase, and heart rate. Static data (0 bpm) was omitted as no motion was present, and thus did not provide an adequate comparison. A p value less than 0.05 was considered significant. Because three-way ANOVAs revealed a three-way interaction effect, additional simple two-way ANOVAs were utilized to determine the effect of acquisition mode and heart rate for each cardiac phase. A p-value of 0.025 was the metric of significance after Bonferroni correction. Simple main effects via one-way ANOVA were also performed to separate two-way interaction effects by evaluating the effect of heart rate for combinations of acquisition mode and cardiac phase. A p-value less than 0.0167, which was adjusted for Bonferroni correction, was considered significant and reported. All statistical analysis was performed in R (R Core Team) and RStudio (RStudio Team).

Results

FWHM. FWHM at different heart rates and acquisition modes demonstrated consistency across different spectral results and cardiac phases (Fig. 4, Table 2). This consistency is demonstrated by the small average differences from the static FWHM of − 0.20, − 0.28, and − 0.15 mm for VMI 150 keV of flash, sequence, and spiral

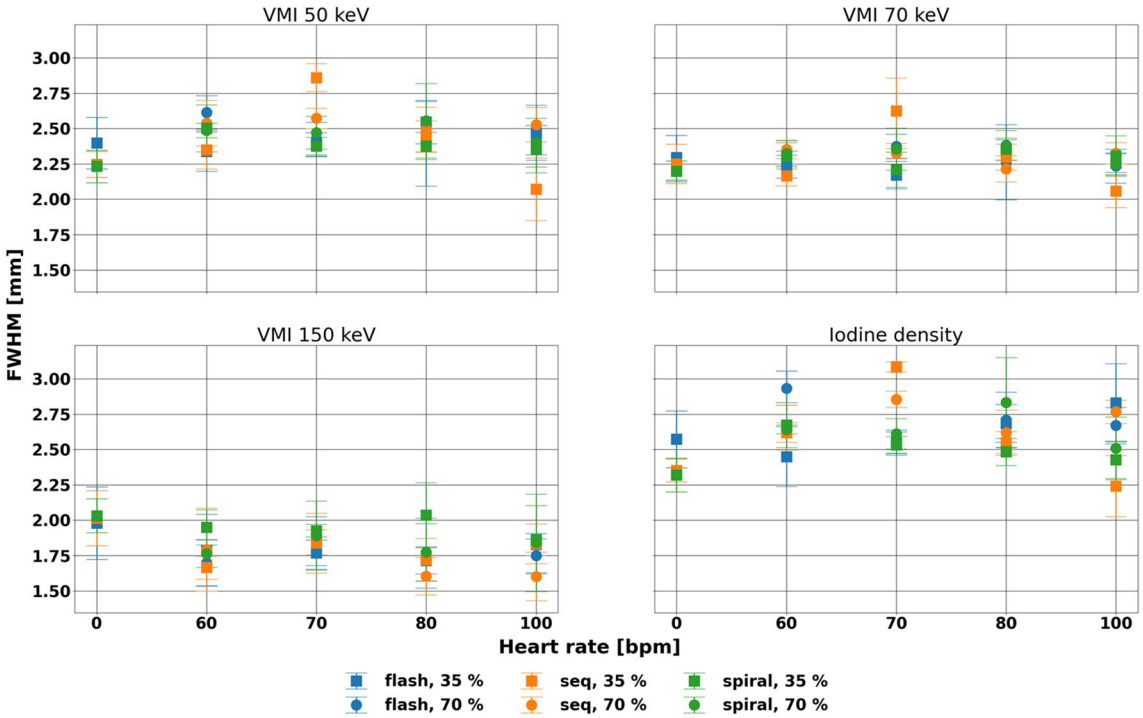

Figure 4. Consistency of full width half max (FWHM) for line profile of stenosed region with various parameters. FWHM varied with heart rate at systole for VMI 50, 70 keV, and iodine density maps but not vary with heart rate or acquisition mode at diastole for all four spectral results. Differences from the static measurements were small at a maximum of 13%.

		FWHM (mm)											
		Flash				Sequence				Spiral			
		35%		70%		35%		70%		35%		70%	
Spectral result	Heart rate (bpm)	Mean	stdev	Mean	stdev	Mean	stdev	Mean	stdev	Mean	stdev	Mean	stdev
VMI 50 keV	0	2.40	0.18	–	–	2.25	0.09	–	–	2.23	0.11	–	–
	60	2.34	0.14	2.62	0.12	2.35	0.13	2.54	0.16	2.50	0.17	2.49	0.05
	70	2.39	0.08	2.42	0.12	2.86	0.10	2.57	0.07	2.38	0.06	2.47	0.12
	80	2.55	0.15	2.39	0.30	2.44	0.11	2.49	0.16	2.38	0.10	2.56	0.26
	100	2.47	0.19	2.42	0.10	2.07	0.22	2.53	0.12	2.36	0.17	2.40	0.17
VMI 70 keV	0	2.29	0.16	–	–	2.25	0.14	–	–	2.20	0.07	–	–
	60	2.23	0.08	2.30	0.05	2.17	0.07	2.35	0.06	2.31	0.09	2.32	0.09
	70	2.17	0.10	2.37	0.09	2.63	0.23	2.33	0.03	2.21	0.12	2.36	0.15
	80	2.35	0.07	2.26	0.27	2.30	0.09	2.22	0.09	2.36	0.08	2.38	0.11
	100	2.26	0.07	2.24	0.12	2.06	0.11	2.32	0.08	2.31	0.14	2.25	0.07
VMI 150 keV	0	1.98	0.26	–	–	2.02	0.19	–	–	2.03	0.12	–	–
	60	1.79	0.25	1.70	0.16	1.67	0.08	1.79	0.29	1.95	0.12	1.76	0.10
	70	1.77	0.09	1.84	0.19	1.84	0.21	1.84	0.09	1.93	0.05	1.89	0.24
	80	1.72	0.10	1.77	0.25	1.72	0.15	1.60	0.13	2.04	0.23	1.77	0.20
	100	1.83	0.08	1.75	0.12	1.83	0.14	1.60	0.17	1.86	0.24	1.84	0.34
Iodine density	0	2.57	0.20	–	–	2.35	0.08	–	–	2.32	0.12	–	–
	60	2.45	0.21	2.93	0.12	2.62	0.07	2.66	0.16	2.67	0.16	2.64	0.03
	70	2.55	0.08	2.55	0.09	3.08	0.04	2.86	0.06	2.53	0.06	2.61	0.11
	80	2.69	0.13	2.71	0.20	2.55	0.08	2.62	0.16	2.48	0.10	2.83	0.32
	100	2.83	0.28	2.67	0.13	2.24	0.22	2.77	0.08	2.43	0.13	2.51	0.22

Table 2. Full width half max for different spectral results at varying heart rates, cardiac phase, and acquisition modes.

scans, respectively, and reflected that the size of the stenosis was preserved at different parameters. The size of the rod did not vary much, with average differences ranging from − 0.02 to 0.32 mm and larger differences seen on iodine density maps.

Statistical testing corroborated that there was no effect of heart rate and acquisition mode at diastole (p-values less than 0.001). In particular, the effect of heart rate was not significant for spiral 35%, flash 70%, sequence 70%, and spiral 70% for each of the spectral results. While other parameters demonstrated significant effect with heart rate, differences in FWHM were small, corresponding to a maximal 13% difference from the static measurements. Despite the consistency for each spectral result, the overall magnitude of the FWHM was smaller for VMI 150 keV (1.8 ± 0.2 mm) in comparison to other spectral results (2.4 ± 0.1, 2.3 ± 0.1, and 2.6 ± 0.1 mm for VMI 50 keV, VMI 70 keV, and iodine density maps, respectively). The difference corresponded to the reduced contrast of the iodine-containing lumen in VMI 150 keV, isolating the stenosis compared to other spectral results.

Dice score. DSC proved mostly similar for each spectral result and acquisition mode with respect to heart rate but showed larger differences at systole and with flash scans (Fig. 5, Table 3). Across acquisition mode, cardiac phase, and heart rate, standard deviation measured 0.08, 0.09, 0.11, and 0.08 for VMI 50, 70, and 150 keV, and iodine density maps, respectively. Specifically, for VMI 150 keV, where the stenosed region was best separated from the lumen, DSC maintained its value across dynamic scans with standard deviations spanning 0.14, 0.15, 0.11, 0.09, 0.10, and 0.08 for flash 35%, flash 70%, sequence 35%, sequence 70%, spiral 35%, and spiral 70%, respectively. The minor effect of acquisition mode was also exhibited for VMI 50 and 70 keV, and iodine density maps. Notably, some of the variation for each acquisition mode and cardiac phase combination can be attributed to specifically a heart rate of 80 bpm rather than higher heart rates, which can be observed both qualitatively and quantitatively. While DSC significantly differed among acquisition modes for different cardiac phases and spectral results, the effect of heart rate was not significant for spiral 35%, sequence 70%, and spiral 70% for any evaluated spectral results (p-values < 0.01), demonstrating the stability at diastole and with spiral mode, with larger differences in systole and with flash scans.

Eccentricity. Similarly, shape of the rod in non-stenosed regions as represented by eccentricity remained stable at different heart rates and acquisition modes at varying cardiac phase and spectral results (Fig. 6, Table 4). Across parameters, eccentricity differences from the static scan averaged 0.012, − 0.021, and 0.103 for VMI 50 and 70 keV and iodine density maps, respectively. At VMI 70 keV, the range of differences relative to the static value at diastole were 0.121, 0.274, and 0.168 for flash, sequence, and spiral, indicating that similarity to the static scan depends on acquisition mode. Furthermore, at systole, ranges were larger at 0.157, 0.224, and 0.183 for flash, sequence, and spiral, respectively. Even though eccentricity was dependent on heart rate for 3/3 and 2/3 of the evaluated spectral results (VMI 50 keV, VMI 70 keV, iodine density maps) at systole and diastole, respectively, the effect of acquisition mode was only present with 1/3 and 0/3 spectral results at systole and diastole, respectively. In particular, heart rate had a significant effect on eccentricity for sequence 35% at VMI 50 keV,

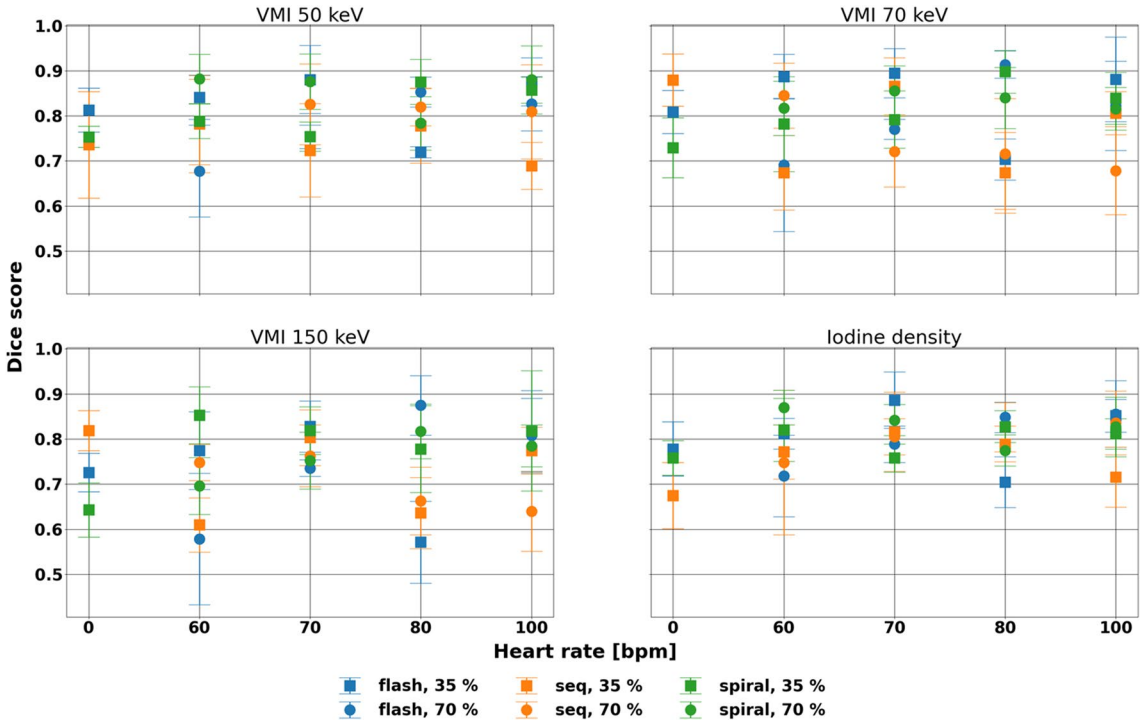

Figure 5. Stability of Dice score of the stenosed region for different spectral results. Dice score demonstrated different primarily associated with heart rate at systole. Clear variation in Dice score at 80 bpm was present, particularly for VMI 70 and 150 keV.

Spectral result	Heart rate (bpm)	Dice score											
		Flash				Sequence				Spiral			
		35%		70%		35%		70%		35%		70%	
		Mean	stdev	Mean	stdev	Mean	stdev	Mean	stdev	Mean	stdev	Mean	stdev
VMI 50 keV	0	0.81	0.05	–	–	0.74	0.12	–	–	0.75	0.02	–	–
	60	0.84	0.05	0.68	0.10	0.78	0.11	0.79	0.09	0.79	0.04	0.88	0.05
	70	0.88	0.08	0.75	0.03	0.72	0.10	0.83	0.09	0.75	0.03	0.88	0.06
	80	0.72	0.01	0.85	0.03	0.78	0.08	0.82	0.04	0.88	0.05	0.78	0.06
	100	0.88	0.05	0.83	0.06	0.69	0.05	0.81	0.10	0.86	0.03	0.88	0.08
VMI 70 keV	0	0.81	0.05	–	–	0.88	0.06	–	–	0.73	0.07	–	–
	60	0.89	0.05	0.69	0.15	0.67	0.08	0.85	0.07	0.78	0.10	0.82	0.06
	70	0.89	0.05	0.77	0.02	0.87	0.06	0.72	0.08	0.79	0.06	0.86	0.06
	80	0.70	0.05	0.91	0.03	0.67	0.09	0.72	0.12	0.90	0.05	0.84	0.07
	100	0.88	0.09	0.82	0.10	0.81	0.05	0.68	0.10	0.84	0.06	0.82	0.05
VMI 150 keV	0	0.73	0.04	–	–	0.82	0.04	–	–	0.64	0.06	–	–
	60	0.77	0.09	0.58	0.15	0.61	0.06	0.75	0.04	0.85	0.06	0.70	0.06
	70	0.83	0.06	0.74	0.02	0.80	0.06	0.76	0.07	0.82	0.05	0.75	0.06
	80	0.57	0.09	0.88	0.07	0.64	0.08	0.66	0.08	0.78	0.10	0.82	0.06
	100	0.82	0.09	0.81	0.08	0.77	0.05	0.64	0.09	0.82	0.13	0.79	0.05
Iodine density	0	0.78	0.06	–	–	0.67	0.07	–	–	0.76	0.04	–	–
	60	0.81	0.03	0.72	0.09	0.77	0.06	0.75	0.16	0.82	0.07	0.87	0.04
	70	0.89	0.06	0.79	0.04	0.82	0.09	0.81	0.04	0.76	0.03	0.84	0.03
	80	0.70	0.06	0.85	0.03	0.79	0.04	0.83	0.05	0.83	0.04	0.77	0.03
	100	0.85	0.04	0.86	0.07	0.72	0.07	0.84	0.07	0.81	0.03	0.83	0.07

Table 3. Dice score for different spectral results at different heart rates, acquisition modes, and cardiac phases.

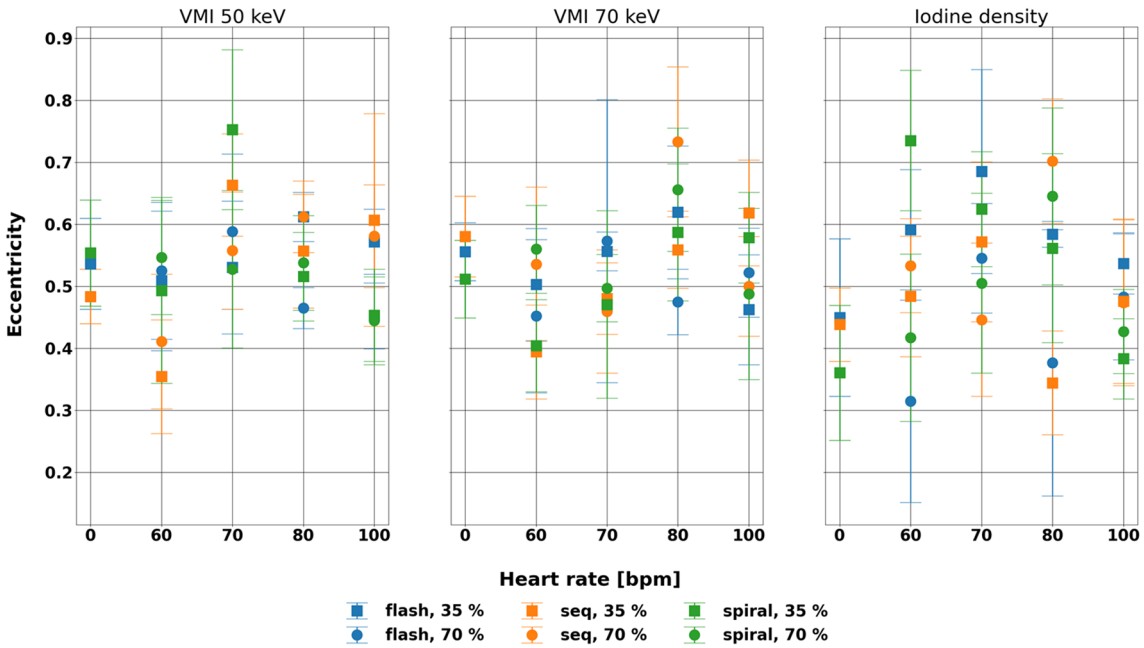

Figure 6. Eccentricity of the non-stenosed region of the rod at different spectral results for different acquisition mode, phase, and heart rate. Eccentricity was not affected by acquisition mode at both systole and diastole while was affected by heart rate, especially for sequence 35% at VMI 50 keV, spiral 35% at VMI 50 keV, and sequence 70% at VMI 70 keV and iodine density maps.

Spectral result	Heart rate (bpm)	Eccentricity											
		Flash				Sequence				Spiral			
		35%		70%		35%		70%		35%		70%	
		Mean	stdev	Mean	stdev	Mean	stdev	Mean	stdev	Mean	stdev	Mean	stdev
VMI 50 keV	0	0.54	0.07	–	–	0.48	0.04	–	–	0.55	0.09	–	–
	60	0.51	0.11	0.53	0.11	0.35	0.09	0.41	0.11	0.49	0.15	0.55	0.09
	70	0.53	0.11	0.59	0.13	0.66	0.08	0.56	0.09	0.75	0.13	0.53	0.13
	80	0.61	0.04	0.47	0.03	0.56	0.09	0.61	0.06	0.52	0.07	0.54	0.08
	100	0.57	0.05	0.45	0.05	0.61	0.17	0.58	0.08	0.45	0.07	0.44	0.07
VMI 70 keV	0	0.56	0.05	–	–	0.58	0.06	–	–	0.51	0.06	–	–
	60	0.50	0.09	0.45	0.12	0.39	0.08	0.54	0.12	0.40	0.07	0.56	0.07
	70	0.56	0.03	0.57	0.23	0.48	0.06	0.46	0.10	0.47	0.15	0.50	0.05
	80	0.62	0.11	0.47	0.05	0.56	0.06	0.73	0.12	0.59	0.11	0.66	0.10
	100	0.46	0.09	0.52	0.07	0.62	0.09	0.50	0.08	0.58	0.07	0.49	0.14
Iodine density	0	0.45	0.13	–	–	0.44	0.06	–	–	0.36	0.11	–	–
	60	0.59	0.10	0.31	0.16	0.48	0.10	0.53	0.08	0.74	0.11	0.42	0.13
	70	0.69	0.16	0.55	0.09	0.57	0.13	0.45	0.12	0.62	0.09	0.50	0.15
	80	0.58	0.02	0.38	0.21	0.34	0.08	0.70	0.10	0.56	0.15	0.65	0.14
	100	0.54	0.05	0.48	0.10	0.48	0.13	0.47	0.13	0.38	0.06	0.43	0.07

Table 4. Eccentricity with varying spectral results, heart rates, acquisition modes, and cardiac phases.

spiral 35% at VMI 50 keV, and sequence 70% at VMI 70 and iodine density maps (p-values < 0.01). Even so, differences in eccentricity remained small compared to eccentricity with static scans.

Discussion

Spectral results exhibited stability with heart rate and acquisition modes at different cardiac phases. The PCCT scanner improves upon existing dual-source dual energy CT with the addition of spectral results while maintaining the image quality available with dual-source CT. This systematic evaluation of the effect of heart rate and acquisition mode on spectral results provides confidence in the reliability of spectral imaging in cardiac CT exams.

With the addition of energy discriminating detectors to dual source CT in the first clinical PCCT, its performance for cardiac CT with respect to heart rate and phase was similar to previous generations of dual source CTs. In spiral mode with second generation dual source CT, the optimal cardiac phase for reconstruction peaked at 30% and 80% between 50 and 100 bpm with measurement overestimation for diameter ranging from 0.1 to 0.4 mm depending on the stenosis size, comparable to FWHM variation across all phase and acquisition mode combinations with PCCT (0.003–0.37 mm)[20]. In particular, for heart rates less than 70 bpm, reconstructions at 70% performed the best with the least motion artifact compared to other evaluated phases[8], while at higher heart rates, there is competing data in regards to the optimal phase[8,20]. While we did not directly evaluate motion artifacts and investigated various spectral results rather than conventional images in this study, results at diastole demonstrated consistent size and shape across heart rate and additionally at systole with spiral mode with the exception of eccentricity at VMI 50 keV. For flash mode, diagnostic image quality was previously reported to be available up to 75 bpm with more artifacts at higher heart rates with lower dose[21]. Likewise, quantitative evaluation via FWHM, DSC, and eccentricity exhibited variation with heart rate with flash, both at diastole and systole, with deviations at higher heart rates. The notable variation at 80 bpm can be attributed to a well-known effect that cardiac motion is reduced at heart rates greater than 80 bpm[22]. The performance with respect to heart rate highlights that the temporal resolution benefits of dual source PCCT were comparable but with the additional availability of spectral results.

While spectral results have been available with other CT technology, the combination of dual source and photon counting CT enables spectral results at higher temporal and spatial resolution in addition to radiation dose reduction. The stability of VMI 50, 70, and 150 keV, and iodine density maps can be extended to other spectral results because of their relation to each other and provides confidence in both quantification and visualization of coronary arteries and other structures. In particular, these spectral results are important for coronary CT angiography, which has increasingly played a role in diagnostic cardiac imaging over invasive angiography[4,23,24]. Both VMIs and effective atomic number maps can characterize the composition of the plaque, i.e. calcification, fibro-fat, and fat, and help better estimate the extent of obstruction for calcified plaques that previously were overestimated as a result of calcium blooming[18,25]. Reduction of calcium blooming artifacts may also permit the evaluation of myocardial ischemia that may result from coronary obstruction, which previously was limited by such artifacts and motion artifacts[26]. Newly developed spectral results, including virtual non-iodine and virtual non-calcium images, may also further improve separation of calcified plaques and the contrast-filled lumen[27]. Generally, accurate identification and categorization of the plaque may guide more refined risk stratification and improve clinical care.

Besides plaque visualization and characterization, spectral results also enable improvement of other cardiovascular applications. In addition to traditional evaluation of coronary artery stenosis with coronary CT angiography, it was feasible to perform calcium scoring with virtual non contrast images from coronary CT angiography, eliminating the need for a dedicated/true non-contrast scan as a result of good image quality and accurate quantification[17,28]. Late iodine enhancement cardiac CT in both dual-layer CT and PCCT illustrated good agreement with magnetic resonance imaging in terms of both visualization with VMI and iodine density maps and quantification of the extracellular volume important for evaluating myocardial fibrosis, edema, and viability in cardiomyopathy[14,15]. Virtual non contrast images, on the other hand, have exhibited improved preservation of stent and calcified structures compared to conventional CT for the surveillance post endovascular aneurysm repair[29]. With the consistency of the spectral results of dual source PCCT, these applications can be investigated and implemented to improve cardiovascular diagnostics.

This study was limited in a few ways. First, in comparison to other studies, the analyzed stenosed region included a calcified stenosis similar in attenuation at low keVs to the lumen and, thus, low in contrast. The lumen and stenosis were best separated on VMI 150 keV as a result of the reduction in the contrast of the lumen in comparison to the stenosis. This provided a more challenging task for evaluating image quality and structural preservation and prevented evaluation of non-stenosed regions on VMI 150 keV. However, it demonstrated the advantages of spectral results, which highlighted the stenosis. Other studies have evaluated stenoses at standard 200, 400, and 800 mg/mL of hydroxyapatite either isolated or at lower background attenuation (200 HU), which provide more contrast[10]. Second, while the motion of the phantom was modeled off Achenbach et al., the phantom did not properly replicate cardiac motion at high heart rates (> 80 bpm) where cardiac motion reduces rather than increases. Despite this, the phantom provided flexibility with inserts comprising of stenoses of different materials and extents. A single clinically relevant stenosis was only analyzed in this study to demonstrate the stability of spectral results. Third, only one phantom size was investigated in this study. Different patient habitus may affect quantification as has been demonstrated with static phantoms, but it is unknown how it may affect dynamic scans. Additionally, this study utilized only a tube voltage of 120 kVp and did not include a tube voltage of 140 kVp. However, both phantom and patient studies have demonstrated excellent image quality and accurate spectral reconstructions[30].

In conclusion, heart rate and acquisition mode did not affect the size of the stenosis, similarity to the static scan, and shape of the non-stenosed region at diastole for different spectral results. With improved material characterization and quantification, these spectral results may ultimately contribute to the advancement of cardiovascular diagnostics via enhanced cardiac CT imaging protocols.

Data availability

Dataset generated during this study are available from the corresponding author upon reasonable request.

Received: 9 May 2023; Accepted: 4 September 2023
Published online: 09 September 2023

References

1. Tsao, C. W. *et al.* Heart disease and stroke statistics-2022 update: A report from the American Heart Association. *Circulation* **145**(8), E153–E639. https://doi.org/10.1161/CIR.0000000000001052 (2022).
2. Sandfort, V. & Bluemke, D. A. CT calcium scoring. History, current status and outlook. *Diagn. Interv. Imaging.* **98**(1), 3–10. https://doi.org/10.1016/J.DIII.2016.06.007 (2017).
3. Knez, A. *et al.* Usefulness of multislice spiral computed tomography angiography for determination of coronary artery stenoses. *Am. J. Cardiol.* **88**(10), 1191–1194. https://doi.org/10.1016/S0002-9149(01)02060-4 (2001).
4. Neumann, F. J. *et al.* 2019 ESC Guidelines for the diagnosis and management of chronic coronary syndromes. *Eur. Heart J.* **41**(3), 407–477. https://doi.org/10.1093/EURHEARTJ/EHZ425 (2020).
5. Maurovich-Horvat, P. *et al.* CT or invasive coronary angiography in stable chest pain. *N. Engl. J. Med.* **386**(17), 1591–1602. https://doi.org/10.1056/nejmoa2200963 (2022).
6. Hsieh, J. *et al.* Step-and-shoot data acquisition and reconstruction for cardiac X-ray computed tomography. *Med. Phys.* **33**(11), 4236–4248. https://doi.org/10.1118/1.2361078 (2006).
7. Flohr, T. G. *et al.* First performance evaluation of a dual-source CT (DSCT) system. *Eur. Radiol.* **16**(2), 256–268. https://doi.org/10.1007/s00330-005-2919-2 (2006).
8. Achenbach, S. *et al.* Influence of heart rate and phase of the cardiac cycle on the occurrence of motion artifact in dual-source CT angiography of the coronary arteries. *J. Cardiovasc. Comput. Tomogr.* **6**(2), 91–98. https://doi.org/10.1016/J.JCCT.2011.11.006 (2012).
9. Flohr, T. G. *et al.* Dual-source spiral CT with pitch up to 3.2 and 75 ms temporal resolution: Image reconstruction and assessment of image quality. *Med. Phys.* **36**(12), 5641–5653. https://doi.org/10.1118/1.3259739 (2009).
10. Eberhard, M. *et al.* Coronary calcium scoring with first generation dual-source photon-counting CT—First evidence from phantom and in-vivo scans. *Diagnostics.* **11**(9), 1708. https://doi.org/10.3390/diagnostics11091708 (2021).
11. Decker, J. A. *et al.* Low-dose CT of the abdomen: Initial experience on a novel photon-counting detector CT and comparison with energy-integrating detector CT. *Eur. J. Radiol.* **148**, 110181. https://doi.org/10.1016/J.EJRAD.2022.110181 (2022).
12. Liu, L. P. *et al.* First-generation clinical dual-source photon-counting CT: ultra-low dose quantitative spectral imaging. *medRxiv.* https://doi.org/10.1101/2021.11.17.21266432 (2021).
13. Rajendran, K. *et al.* First clinical photon-counting detector CT system: Technical evaluation. *Radiology* **303**(1), 130–138. https://doi.org/10.1148/RADIOL.212579 (2022).
14. Oda, S. *et al.* Myocardial late iodine enhancement and extracellular volume quantification with dual-layer spectral detector dual-energy cardiac ct. *Radiol. Cardiothorac. Imaging.* **1**(1), 180003. https://doi.org/10.1148/RYCT.2019180003/ASSET/IMAGES/LARGE/RYCT.2019180003.FIG4B.JPEG (2019).
15. Mergen, V. *et al.* Extracellular volume quantification with cardiac late enhancement scanning using dual-source photon-counting detector CT. *Investig. Radiol.* **57**(6), 406–411. https://doi.org/10.1097/RLI.0000000000000851 (2022).
16. Wang, Q., Shi, G., Qi, X., Fan, X. & Wang, L. Quantitative analysis of the dual-energy CT virtual spectral curve for focal liver lesions characterization. *Eur. J. Radiol.* **83**(10), 1759–1764. https://doi.org/10.1016/J.EJRAD.2014.07.009 (2014).

17. Yamada, Y. *et al.* Feasibility of coronary artery calcium scoring on virtual unenhanced images derived from single-source fast kVp-switching dual-energy coronary CT angiography. *J. Cardiovasc. Comput. Tomogr.* **8**(5), 391–400. https://doi.org/10.1016/J.JCCT.2014.08.005 (2014).
18. Van Hedent, S. *et al.* Effect of virtual monoenergetic images from spectral detector computed tomography on coronary calcium blooming. *J. Comput. Assist. Tomogr.* **42**(6), 912–918. https://doi.org/10.1097/RCT.0000000000000811 (2018).
19. Achenbach, S. *et al.* In-plane coronary arterial motion velocity: Measurement with electron-beam CT. *Radiology* **216**(2), 457–463. https://doi.org/10.1148/RADIOLOGY.216.2.R00AU19457/ASSET/IMAGES/LARGE/R00AU19L6X.JPEG (2000).
20. Lell, M. M. *et al.* Evaluation of coronary stents and stenoses at different heart rates with dual source spiral CT (DSCT). *Investig. Radiol.* **42**(7), 536–541. https://doi.org/10.1097/RLI.0B013E318041F674 (2007).
21. Morsbach, F. *et al.* Performance of turbo high-pitch dual-source CT for coronary CT angiography: First ex vivo and patient experience. *Eur. Radiol.* **24**(8), 1889–1895. https://doi.org/10.1007/S00330-014-3209-7/FIGURES/5 (2014).
22. Petersilka, M., Bruder, H., Krauss, B., Stierstorfer, K. & Flohr, T. G. Technical principles of dual source CT. *Eur. J. Radiol.* **68**(3), 362–368. https://doi.org/10.1016/J.EJRAD.2008.08.013 (2008).
23. Giusca, S. *et al.* Coronary computer tomography angiography in 2021—Acquisition protocols, tips and tricks and heading beyond the possible. *Diagnostics.* **11**(6), 1072. https://doi.org/10.3390/diagnostics11061072 (2021).
24. Newby, D. *et al.* Coronary CT angiography and 5-year risk of myocardial infarction. *N. Engl. J. Med.* **379**(10), 924–933. https://doi.org/10.1056/NEJMOA1805971 (2018).
25. Nakajima, S. *et al.* Clinical application of effective atomic number for classifying non-calcified coronary plaques by dual-energy computed tomography. *Atherosclerosis* **261**, 138–143. https://doi.org/10.1016/J.ATHEROSCLEROSIS.2017.03.025 (2017).
26. Carrascosa, P. M. *et al.* Comparison of myocardial perfusion evaluation with single versus dual-energy CT and effect of beam-hardening artifacts. *Acad. Radiol.* **22**(5), 591–599. https://doi.org/10.1016/J.ACRA.2014.12.019 (2015).
27. Emrich, T. *et al.* Coronary computed tomography angiography-based calcium scoring: In vitro and in vivo validation of a novel virtual noniodine reconstruction algorithm on a clinical, first-generation dual-source photon counting-detector system. *Investig. Radiol.* **57**(8), 536–543. https://doi.org/10.1097/RLI.0000000000000868 (2022).
28. Gassert, F. G. *et al.* Calcium scoring using virtual non-contrast images from a dual-layer spectral detector CT: Comparison to true non-contrast data and evaluation of proportionality factor in a large patient collective. *Eur. Radiol.* **31**(8), 6193–6199. https://doi.org/10.1007/S00330-020-07677-W (2021).
29. Decker, J. A. *et al.* Virtual non-contrast reconstructions of photon-counting detector CT angiography datasets as substitutes for true non-contrast acquisitions in patients after EVAR-performance of a novel calcium-preserving reconstruction algorithm. *Diagnostics (Basel, Switzerland).* https://doi.org/10.3390/DIAGNOSTICS12030558 (2022).
30. Rajendran, K. *et al.* Dose reduction for sinus and temporal bone imaging using photon-counting detector CT with an additional tin filter. *Investig. Radiol.* **55**(2), 91. https://doi.org/10.1097/RLI.0000000000000614 (2020).

Acknowledgements

We acknowledge support from Siemens Healthineers and NIH (R01EB030494).

Author contributions

Conception: L.L., N.S., M.C., P.S., P.N. Design: L.L., N.S., P.N. Data acquisition: L.L. Analysis: L.L. Drafting: L.L. Revising: L.L., N.S., P.S., F.K., G.G., M.C., H.L., P.N.

Competing interests

HL and PN have a research agreement with Siemens Healthineers. PS is an employee of Siemens Healthineers. The other authors have no relevant conflicts of interests to disclose.

Additional information

Correspondence and requests for materials should be addressed to L.P.L. or P.B.N.